PAPER

Microtexture, microstructure evolution, and thermal insulation properties of Si₃N₄/silica aerogel composites at high temperatures

Haixia Yang [ID] *[a] and Feng Ye[b]

Insights into the micro-texture, micro-morphology, and pore structure of Si_3N_4/SiO_2 aerogel composites at high temperatures are presented. At high heat treatment temperatures, the silica aerogel inside the composite material gradually crystallised, and the fusion of micropores caused the decrease of pores and the increase of pore size. Compared with the pure SiO_2 aerogel, Si_3N_4 particles embedded in the nano-network structure provided effective support and hindered the aerogel crystallisation at high temperatures. To reduce the radiative thermal conductivity, Si_3N_4/silica aerogel composites were doped with the opacifier TiO_2. At higher TiO_2 content, the thermal diffusivity and thermal conductivity of the composites decreased more slowly below 800 °C, and substantially above 1000 °C. For TiO_2 20 wt%, the measured dielectric constant was 2.85, and the thermal conductivity of the composite decreased by approximately 35% (at 1300 °C). The results show that an appropriate TiO_2 content improved the thermal insulation performance of the composite, but damaged the wave permeability, whereas high contents were unfavourable. This study provides theoretical and technical support for the preparation and application of high temperature wave permeable insulation materials.

Introduction

The continuous hypersonic vehicle renewal and flight Mach number increase led to the wave-permeable component bearing higher temperatures and heat flows to tackle the aerodynamic heat generated by the intense air compression and friction. To ensure a regular communication of the aircraft, the requisites of integrated materials are high temperature resistance, heat insulation, and wave permeability. The recently investigated porous ceramic wave-permeable materials Si_3N_4,[1–3] $SiAlON$,[4] and Si_3N_4/Si_2N_2O (ref. 5) are characterized by lower dielectric constant and dielectric loss, and higher solid-phase thermal conductivity compared with dense wave-permeable ceramics. Nevertheless, due to the synthesis limitations, the larger pore size (μm) than the mean free path of air (∼69 nm) hinders the heat-flow-transfer suppression, resulting in a limited heat insulation performance. Owing to its unique nano-network structure, SiO_2 aerogel features low density (0.03–0.5 g cm⁻³), high porosity (80–99.8%), low thermal conductivity (0.005–0.1 W m⁻¹ K⁻¹), low dielectric constant (1–2), and low dielectric loss (loss Angle tangent 10^{-1} to 10^{-3}).[6–8] The excellent heat insulation and wave permeability allow its exploitation as the

sandwich structure material of wave permeability components, as extensively reported in the aerospace field literature.

Low density and efficient heat insulation require improved SiO_2 aerogel porosity, whereas the constant decrease of solid content reduces its mechanical properties. As an example, pure SiO_2 aerogel with a density of 0.13 g cm⁻³ is damaged under 0.031 MPa pressure;[9] moreover, its ultra-low mechanical strength accelerates fracturing and hampers applications requiring complete-block structures. The mechanical properties of SiO_2 aerogel materials are remarkably enhanced by the addition of polymers with certain mechanical strength.[10–12] However, the operating temperature of organic-polymer-reinforced SiO_2 aerogel composites (≤1000 °C) is limited by the pyrolysis temperature of the organic functional groups. To improve the separation between SiO_2 aerogel and fibre, SiO_2 aerogel composite materials were prepared with reinforcing nanofibers with small diameter, including cellulose, carbon, polyurethane, polyaniline, and SiO_2 nanofibers.[13–21] However, the preparation and dispersion of nanofibers contribute to the SiO_2-aerogel-composite synthesis complexity, with most of the drying process still requiring expensive supercritical drying. Moreover, systematic studies on the transmittance of nano-fibre reinforced SiO_2 aerogel are absent.

The excellent thermal insulation performance of SiO_2 aerogel arises from the nano-network structure formed by the amorphous nanoparticle inter-connection. However, amorphous SiO_2 crystallizes at high temperatures, leading to structural damages and thermal insulation performance

[a]School of Textile and Materials Engineering, Dalian Polytechnic University, Dalian 116034, P. R. China. E-mail: yanghaixiaedu@163.com

[b]School of Materials Science and Engineering, Harbin Institute of Technology, Harbin 150001, P. R. China

degradation. The sintering of pure SiO_2 aerogel above 800 °C affects the heat insulation performance.[22] Research efforts focus on improving the mechanical properties and high temperature resistance of SiO_2 aerogel to promote its practical applications as high temperature resistant, heat insulator and wave permeability integrated material. Particularly, extensive research aimed at improving SiO_2 aerogel thermal stability. As an example, powders and sol precursors, including Al_2O_3, TiO_2, and ZrO_2, and SiO_2 aerogel composites are used to obtain composite materials with service temperature increased to 1000–1100 °C.[23–25] However, the high dielectric constant of these reinforcing materials reduces the wave permeability of the SiO_2 aerogel composites, hampering their applications in the field of wave permeability. Therefore, the selection of the appropriate means and reinforcement materials is crucial to improve the SiO_2 aerogel heat-resistance-temperature and realize the integration of wave permeability and heat insulation function.

Solid phase merger and pore structure collapse during SiO_2 aerogel sintering are detrimental for the thermal insulation performance. In the sintering process of SiO_2 aerogel reported by Jean *et al.*,[26] solid phase merger and pore collapse occurred sequentially. The SiO_2 aerogel high surface energy leads to facile sintering in high temperature environment, resulting in the aerogel pore-structure-collapse and heat insulation performance shrinkage. Therefore, the high-temperature resistance of SiO_2 aerogel should be improved from the perspective of anti-sintering. The network structure retain should be combined with the SiO_2-aerogel-particle-crystallization inhibition. Therefore, appropriate methods improving the thermal stability of SiO_2 aerogel allow complying with the higher temperature requirements.

Owing to the Si_3N_4 excellent temperature resistance and dielectric properties, Si_3N_4 particles were used as reinforcement, and sol–gel method and atmospheric drying process were used to prepare Si_3N_4/SiO_2 aerogel composite materials,[27] resulting in good heat insulation performance and wave permeability. This paper reports the insights into the phase composition and microstructure of Si_3N_4/SiO_2 aerogel composites at high temperatures. Concurrently, TiO_2 was used as sunshade to improve the high-temperature heat insulation performance of the composite materials, providing theoretical and technical support for the preparation and application of high-temperature wave-permeable heat insulation materials.

Experimental procedure

Materials and chemicals

Tetraethoxysilane (98%, AR), ethanol (99%, AR), oxalic acid, isopropanol, polyacrylic acid (LR), *N*,*N*-dimethylformamide (DMF), *n*-hexane, ammonia (30%, AR) were purchased from Sinopharm Chemical Reagent Co., Ltd., China. Si_3N_4 powders (98%, $d = 0.5$ μm) were purchased from UBE Co., Ltd., Japan. TiO_2 powders (99%, $d = 0.5$ μm) were purchased from Sinopharm Chemical Reagent Co., Ltd., China.

Preparation process

The schematic diagram of the sample preparation process is shown in Fig. 1. Tetraethoxysilane was first dissolved in ethanol (molar ratio 1 : 8), and water and oxalic acid solution were subsequently added (with tetraethoxysilane : water : oxalic acid solution molar ratio equal to $1 : 3 : 1 \times 10^{-3}$), with magnetic stirring for 48 h. Water, *N*,*N*-dimethylformamide and ammonia (the molar ratio of tetraethoxysilane to it is $1 : 1 : 1 : 1 \times 10^{-2}$) were then added to obtain the silica sol. Afterwards, a certain volume fraction of Si_3N_4 powder was added to the silica sol system (5, 10, 15, and 20 vol%), with polyacrylic acid (PAA) used as a dispersant according to the mass ratio polyacrylic acid-: powder $Si_3N_4 = 1 : 100$. After stirring evenly, the obtained gel was poured it into a mixing tank with Si_3N_4 balls for wet mixing; after 12 hours, a gel composite containing Si_3N_4 powder was obtained. As a comparison, TiO_2 powder 5 wt%, 10 wt%, 15 wt%, and 20 wt% was added to the sol composite system with 10 vol% of Si_3N_4. The same process was adopted for the wet mixing. After demoulding, the wet gel composite was placed in an ethanol/water mixture (with volume ratio 7 : 3), ethyl orthosilicate/ethanol mixture (with volume ratio 7 : 3), iso-propanol, isopropanol/*n*-hexane mixed solution, and *n*-hexane with a volume ratio of 1 : 1, respectively aging for 24 h at 60 °C, and slowly drying. The dried gel composite was finally heated in an air oven at 200 °C for 2 h (heating rate 5 °C min^{-1}) and then heated at 700 °C for 2 h (heating rate 5 °C min^{-1}) to obtain the Si_3N_4/SiO_2 aerogel composites and TiO_2 containing composites. The obtained samples were treated at 900 °C, 1100 °C, 1200 °C and 1300 °C for 2 h with a heating rate of 5 °C min^{-1} to study the high-temperature microstructure evolution and thermal insulation properties of the materials.

Characterization

The crystalline phase of the material was identified by X-ray diffraction analysis (XRD, Shimadzu XRD-7000S). The microscopic morphology of the samples was characterised by scanning electron microscopy (SEM, Helios Nanolab600i, FEI Co., Oregon, USA). Nitrogen adsorption isotherms were measured by a gas adsorption analyser (Gemini VII 2390, Micrometics Co., USA) at 77 K. The specific surface area and pore size distribution curves of the samples were calculated according to the Brunauer–Emmett–Teller method and Barrett–Joiner–Halenda model, respectively. The dielectric constant and loss tangent were measured by test equipment (Model N5230A, Agilent Technologies USA). The specific heat capacity (C_p, J g^{-1} K^{-1}) was determined by a NETZSCH LFA427 apparatus (Selb, Germany). The thermal diffusivity (α, mm^2 s^{-1}) in the through-plane direction of the samples (diameter 12.6 mm, thickness 2 mm) was measured with a NETZSCH LFA427 apparatus (Selb, Germany) at a heating rate of 10 °C min^{-1}. The thermal conductivity (λ, W m^{-1} K^{-1}) of the specimens was calculated from the density ρ (cm^3 g^{-1}) from eqn (1):

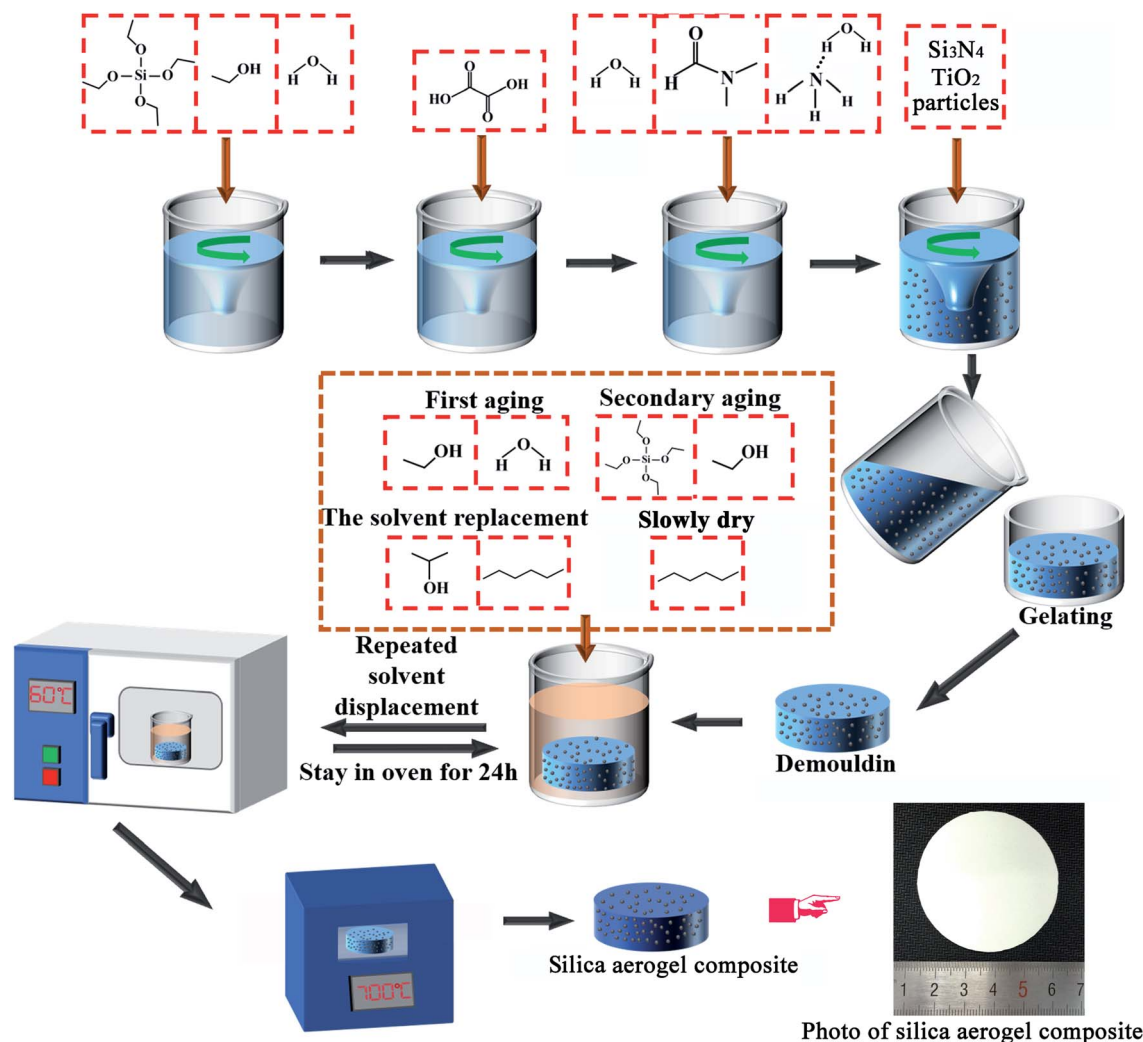$$\lambda = \alpha \times \rho \times C_p \tag{1}$$

Fig. 1 Schematic image of the sample preparation process.

Results and discussion

Micro-texture evolution of Si_3N_4/silica aerogels at high temperatures

The XRD patterns of silica aerogels and Si_3N_4/silica aerogel composites (Si_3N_4 5 vol%) after heat treatment at different temperatures are shown in Fig. 1. As shown in Fig. 2(a), the silica aerogel is amorphous at 900 °C. When the temperature is 1100 °C, the crystal diffraction peak appears in the range of 20–40°, indicating that the silica aerogel has partially crystallized. Above 1200 °C, sharp diffraction peak with high intensity appeared, indicating that silica aerogel had crystallized. The XRD patterns of the composites treated at 700 °C for 2 h show wide diffracted peaks in the 2θ range 20–30°, indicating the amorphous nature of the silica aerogel. At higher treatment temperatures, the diffraction intensity of the bread-like broad peak gradually increased, and the peak gradually became sharper, indicating the progressive silica aerogel crystallization. After the treatment at 1100 °C for 2 h, the diffraction peaks of the composites retained the typical shape of amorphous

species, with some narrowing indicating the gradual crystallization. Additionally, the diffraction peak intensity near 22° is slightly higher than the relative intensity of pure Si_3N_4 diffraction peak at this position, reasonably due to the superimposition of the Si_3N_4 crystal and silica aerogel diffraction peaks. Upon the treatment at 1300 °C for 2 h, most of the crystals crystallized. The highest diffraction intensity was observed at $2\theta = 21.6°$, corresponding to the crystal plane (111), and the corresponding crystal structure was cristobalite. Therefore, the heat treatment temperature increase led to a gradual crystallization of the silica aerogel in the composite, hampering its use for a prolonged time at temperatures above 1300 °C.

Temperature effects on the micro-morphology of Si_3N_4/silica aerogel composites

Photos and SEM images of samples before and after heat treatment at different temperatures are shown in Fig. 3. It can be seen from the photo that the pure aerogel block was broken after heat treatment at 900 °C. With the increase of treatment
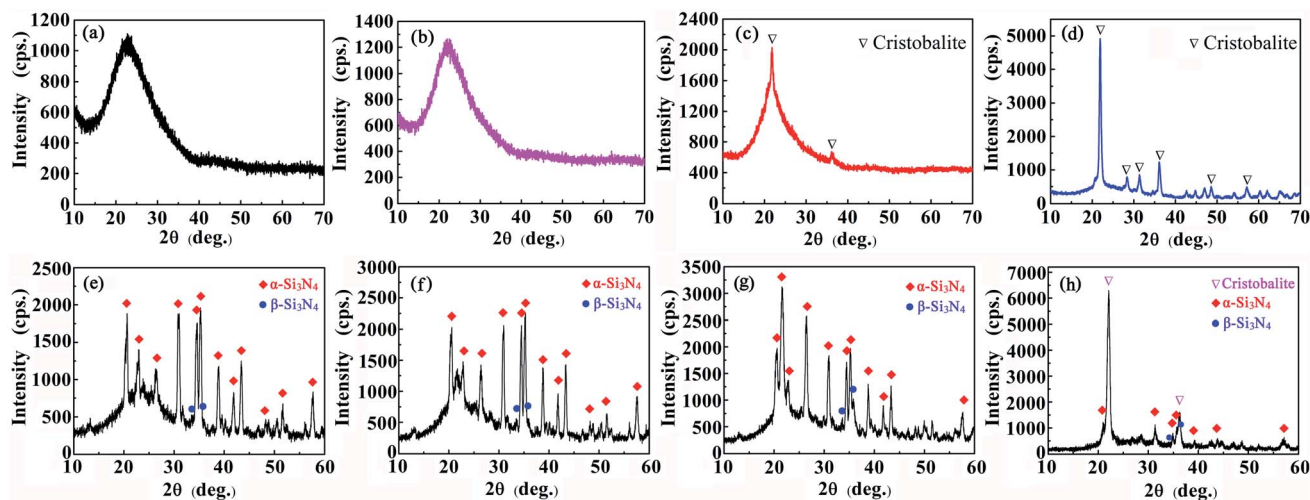
Fig. 2 XRD patterns of silica aerogels (a–d) and Si_3N_4/silica aerogel composites (e–h) heat-treated at different temperatures for 2 h: (a, e) 700 °C; (b, f) 900 °C, (c, g) 1100 °C; (d, h) 1300 °C.

temperature, aerogels gradually crystallized and became dark hard blocks after heat treatment at 1200 °C. By Si_3N_4 particle reinforcement, the composites remained intact at 1300 °C

without cracks. SEM images showed that the pure aerogel had uniform nanoporous structure after heat treatment at 900 °C (Fig. 3(a)), and the pores disappeared after treatment at 1100 °C
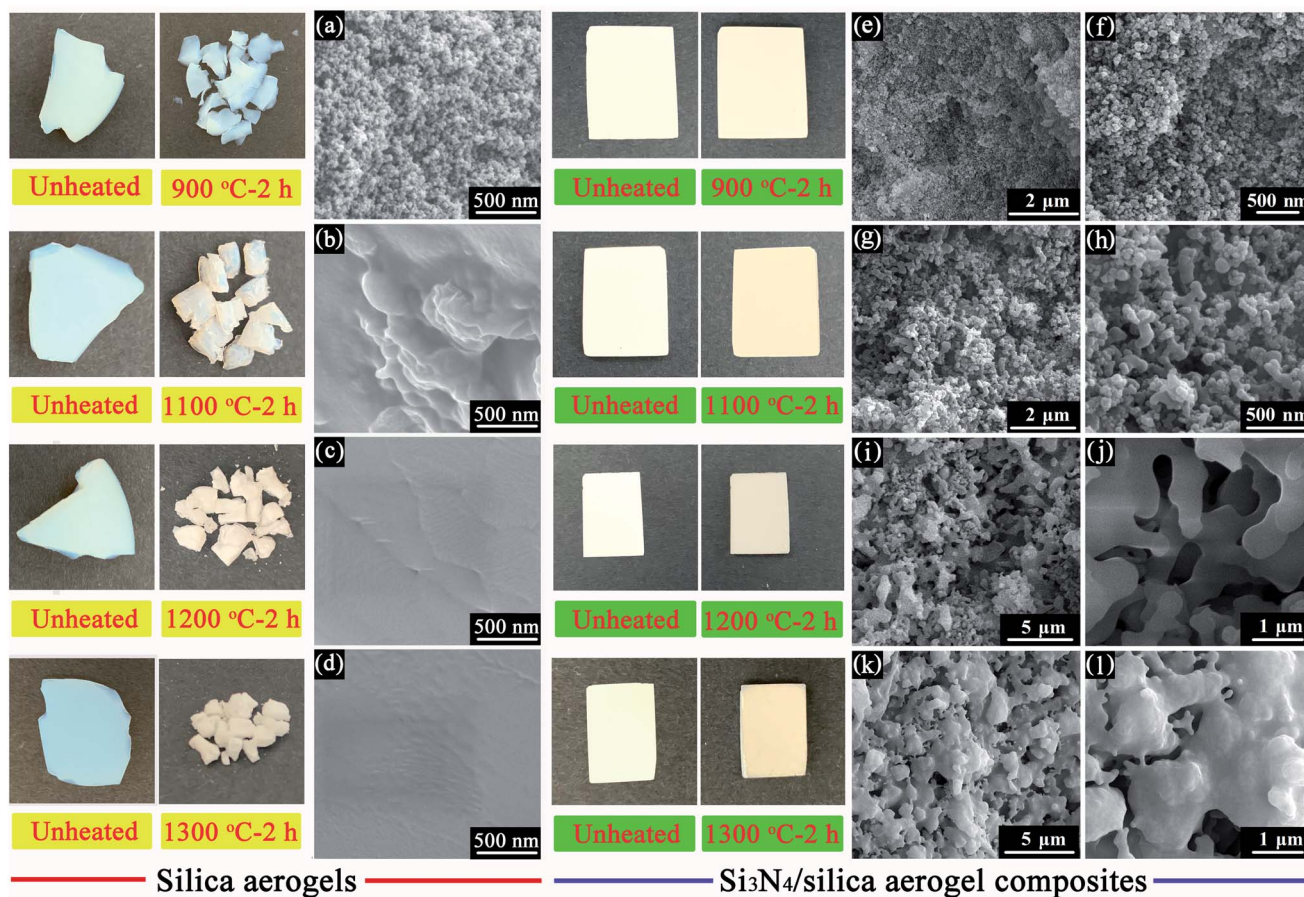

Fig. 3 Photos and SEM images of the silica aerogels heat-treated at different temperatures for 2 h: (a) 900 °C, (b) 1100 °C, (c) 1200 °C, (d) 1300 °C; and Si_3N_4/silica aerogel composites (with Si_3N_4 5 vol%) heat-treated at different temperatures for 2 h: (e, f) 900 °C, (g, h) 1100 °C, (i, j) 1200 °C, (k, l) 1300 °C.

and above (Fig. 3(b)–(d)). After 2 h at 900 °C, the composite network exhibited a uniform structure, and the internal particle and pore size were in the order of tens of nanometres (Fig. 3(e) and (f)). The low-power SEM images of the samples upon increased processing temperature (1100 °C for 2 h) did not show clear cracks in the aerogel, and the particles gradually agglomerated and crystallized. The high-magnification image comparison in Fig. 3(g) and (h) shows a reduction of the pores and increase in the pore size due to the fusion of micropores, with most of the pores still in the nanoscale size. At 1200 °C, the size of the skeleton inside the composite increased, the number of nanopores further decreased, and the micropores merged or disappeared, forming larger size pores (Fig. 3(i) and (j)). Upon 2 h treatment at 1300 °C, most of the silica aerogels crystallized and adhered to the surface of the Si_3N_4 particles (Fig. 3(k) and (l)). The nanopores inside the aerogel mostly disappeared, and limited small pores remained. Therefore, the morphology analysis showed the considerable temperature influence on the microstructure of the Si_3N_4/silica aerogel composites: at 1300 °C, silica aerogel crystallization hinders the nanoporous structure retention.

Temperature effects on the pore structure of Si_3N_4/silica aerogel composites

The nitrogen adsorption isotherms and pore size distributions of the Si_3N_4/silica aerogel composites (Si_3N_4 5 vol%) heat-

Table 1 Pore structure parameters of the composites heat-treated at different temperatures. Thermal insulation performance of Si_3N_4/silica aerogel composites at high temperatures

Temperature (°C)	S_{BET} (m² g⁻¹)	V_{total} (cm³ g⁻¹)	D_{peak} (nm)
Unheated	178	0.478	19.3
700	160	0.433	26.3
900	104	0.302	64.0
1100	27	0.103	108.9
1200	22	0.056	161.3
1300	3	0.053	Multi-peak

treated at different temperatures are shown in Fig. 4, and the corresponding pore structure parameters are summarized in Table 1. As can be seen from the Fig. 4(a), the unheated composite exhibits typical class I–V curve adsorption isotherms, indicating the presence of mesoporous structures. With the increase of treatment temperature, the class I–V curve adsorption isotherm remained unchanged, denoting that the composite retained nanoscale holes due to the support of Si_3N_4 particles, whereas the nitrogen adsorption amount decreased gradually, indicating the quantitative reduction of internal holes in the composite. At higher treatment temperatures, the adsorption isotherm of the composite gradually showed the multi-stage rise typical of a non-uniform pore size distribution. The pore size distribution curve (Fig. 4(b)) shows the pore size
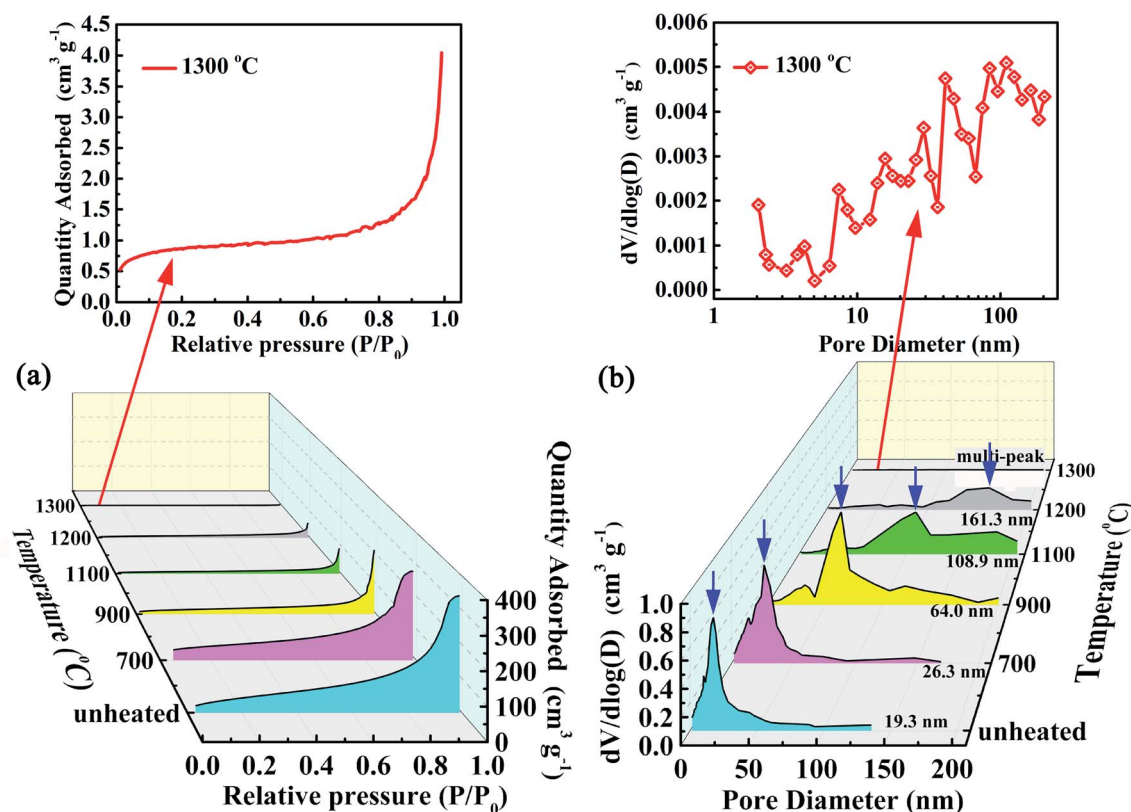

Fig. 4 (a) Nitrogen adsorption isotherms and (b) pore size distributions of the Si_3N_4/silica aerogel composites heat-treated at different temperatures.

distribution peak broadening and shifting toward the larger pore size.

The specific surface area (S_{BET}) and pore volume of the composite material substantially decreased and the pore size gradually increased at higher temperatures (Table 1). In our study, the obtained pure silica aerogel has a high S_{BET} of 790 m^2 g^{-1}, a density of 0.14 g cm^{-3}, and a gel particle size of 10–20 nm.[27] As reinforcement, the particle size of Si_3N_4 is 0.5 μm and the density is 3.18 g cm^{-3}. Due to the large particle size and high density of Si_3N_4, the composite shows a low specific surface area. The S_{BET} of the untreated composite was 178 m^2 g^{-1}, decreased slightly to 160 m^2 g^{-1} at 700 °C for 2 h, decreased to 104 m^2 g^{-1} at 900 °C, and nearly zero at 1300 °C. The combination of the results of XRD (Fig. 2) and SEM (Fig. 3) analyses shows that the aerogel gradually crystallized due to the temperature increase, and the internal micropores collapsed, causing the S_{BET} decrease. Concurrently, the micropore S_{BET}

decreased sharply at higher treatment temperatures, indicating the decrease in number of micropores, consistently with the SEM results. The pore structure resulting from the treatment temperature increasing from 700 °C to 1200 °C showed a predominance of nanopores, although a certain number of macropores was still observed. Under the high temperature environment, silica aerogel crystallises, with a crystallisation degree related to the heat treatment time.

Specific heat capacity, thermal diffusivity, and thermal conductivity of the Si_3N_4/silica aerogel composites with different Si_3N_4 contents are shown in Fig. 5. At room temperatures, the obtained pure silica aerogels could not be made into standard units to test the thermal conductivity. After adding Si_3N_4 particles, the mechanical property of the composites was improved. The thermal conductivity of the composite (with Si_3N_4 content of 5 vol%) is 0.031 W m^{-1} K^{-1}, which is higher than that of the pure aerogel (0.014 W m^{-1} K^{-1}) reported in ref. 28. At higher
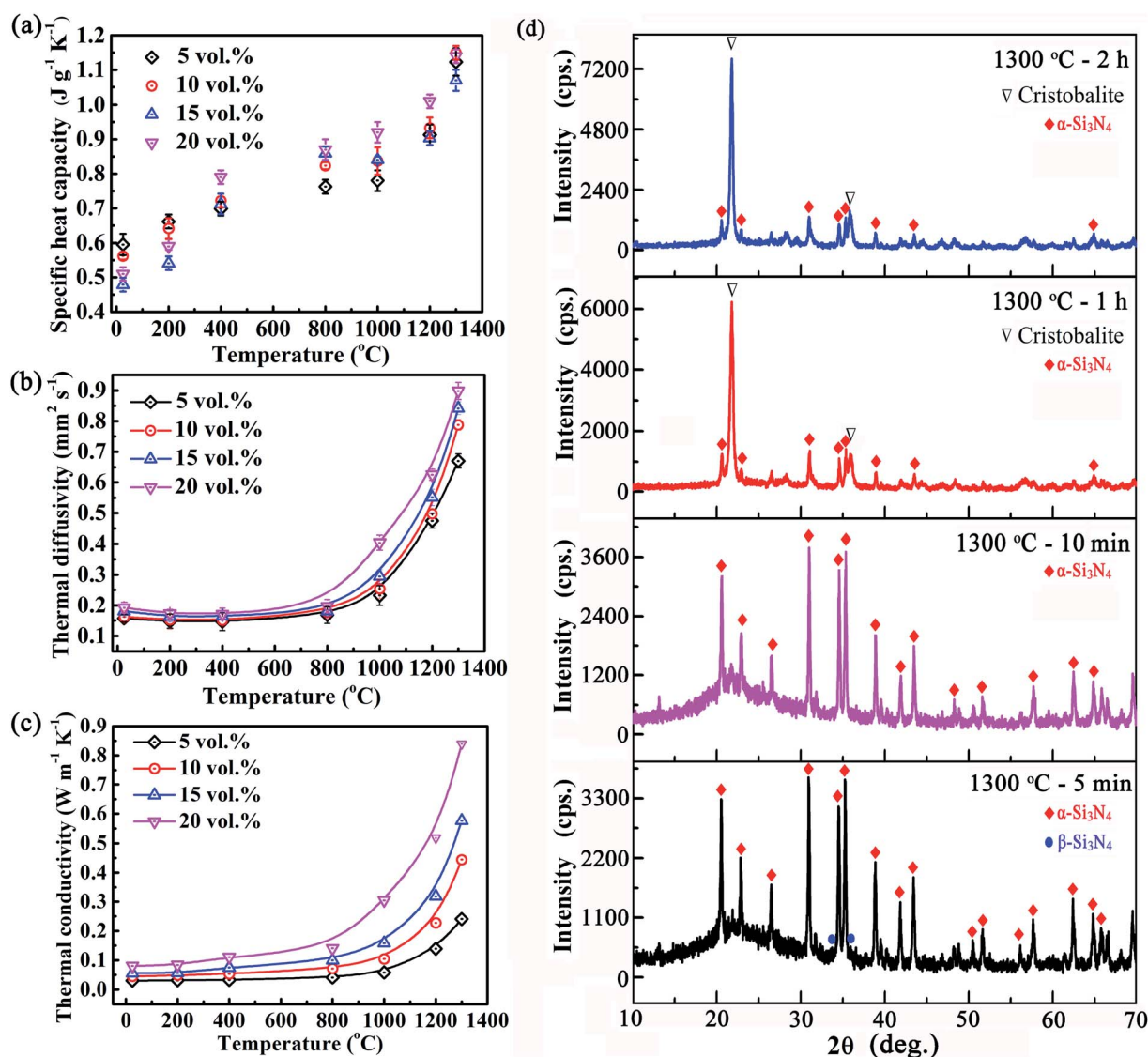

Fig. 5 (a) Specific heat capacity, (b) thermal diffusivity, (c) thermal conductivity and (d) XRD patterns of the Si_3N_4/silica aerogel composites. Dielectric properties of Si_3N_4/silica aerogel composites with different TiO_2 contents at high temperatures.

temperatures, the specific heat capacity of composites gradually increased. At the same temperature, the specific heat capacity values of composites with different Si_3N_4 contents are comparable, indicating the limited influence of Si_3N_4 particle addition on the aerogel structure and the aerogel structure retention. Below 700 °C, the composite structure was stable, and the thermal diffusivity of the composite material remained unchanged at higher temperatures, and then increased gradually with the temperature increase. The thermal diffusivity and thermal conductivity increased sharply at temperatures above 1000 °C. The analysis of the influence of the temperature on the phase structure and microstructure of the composites indicated that S_{BET}, pore size, and porosity decreased at higher temperatures. Concurrently, the aerogel inside the composite gradually crystallized, and the improvement of the order degree increased the heat conduction of the solid phase, leading to thermal diffusion coefficient and thermal conductivity increase. In the thermal diffusivity test, the heating rate is 10 °C min^{-1} and the constant temperature is about several minutes. In order to investigate the effect of holding time on phase transformation of composite materials (with Si_3N_4 10 vol%), the samples were heated to 1300 °C at 10 °C min^{-1} and held for 5 min, 10 min, 1 h and 2 h, respectively. The XRD test results are shown in Fig. 5(d).

It can be seen that the aerogel inside the composite did not completely crystallize after holding for 10 min at 1300, but had completely crystallized after holding for 1 h. Obviously, the rapid heating rate and short constant temperature time resulted in incomplete crystallization of aerogel in the thermal diffusivity test. Therefore, the composite material (with Si_3N_4 10 vol%) exhibited a low thermal conductivity (0.444 W m^{-1} K^{-1}) at 1300 °C.

The dielectric constant and dielectric loss of Si_3N_4/silica aerogel composites doped with different TiO_2 contents showed limited fluctuations as a function of frequency (Fig. 6). The dielectric constant of the composites increased substantially at higher TiO_2 contents, due to the higher TiO_2 powder dielectric constant (approximately 114) than that of Si_3N_4/silica aerogel
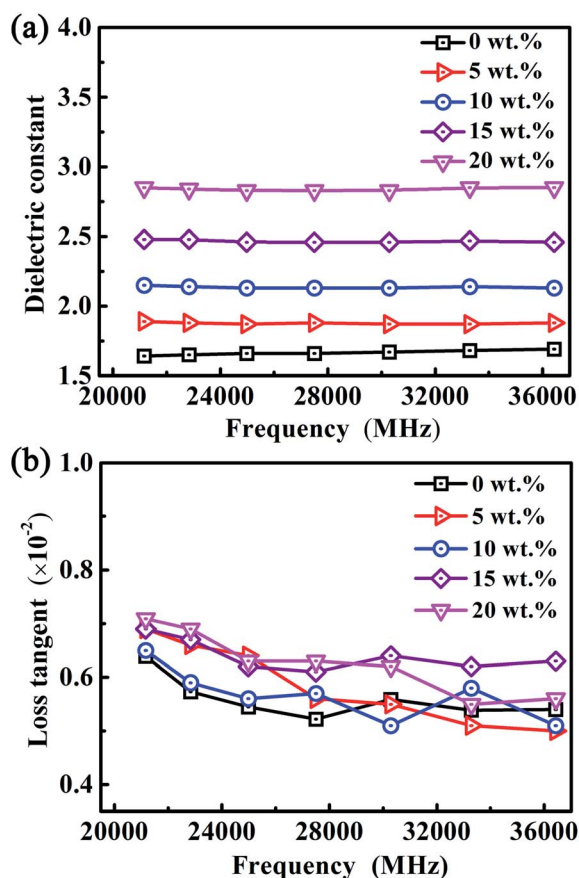

Fig. 6 (a) Dielectric constant and (b) loss tangent of the Si_3N_4/silica aerogel composites with different TiO_2 contents. Thermal insulation performance of Si_3N_4/silica aerogel composites with different TiO_2 contents at high temperatures.
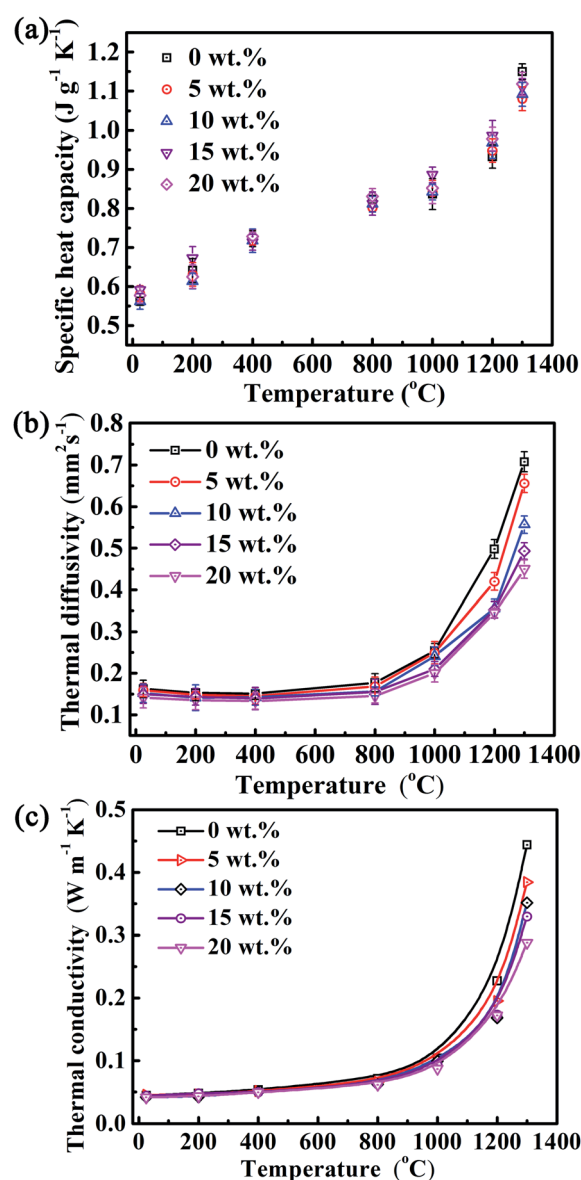

Fig. 7 (a) Specific heat capacity, (b) thermal diffusivity, and (c) thermal conductivity of the Si_3N_4/silica aerogel composites with different TiO_2 contents.

composites (approximately 1.65, Fig. 6(a)). Concurrently, the dielectric loss of the composite material increased due to the scattering of TiO_2 particles (Fig. 6(b)). For TiO_2 20 wt%, the measured dielectric constant was 2.85. Higher TiO_2 contents led to a continuous increase in the dielectric constant. Therefore, the TiO_2 content should be limited, as higher dielectric constants are detrimental to the wave-transmitting properties of the composite material.

The specific heat capacity, thermal diffusivity and thermal conductivity of Si_3N_4/silica aerogel composites doped with different TiO_2 contents varied with the temperature (Fig. 7). At higher TiO_2 contents, the specific heat capacity of the composite material was unaltered, whereas the thermal diffusion coefficient and thermal conductivity gradually decreased, with limited variations below 800 °C and an extensive decreasing range above 1000 °C. At low temperatures, heat conduction is the main heat transfer mode, whereas radiant thermal conductivity accounts for a small proportion, so the change of thermal conductivity is not obvious. At high temperatures, thermal radiation becomes the main heat transfer mode, with the thermal conductivity reduced by the heat scattering and absorption promoted by the TiO_2 particles. At 1300 °C, the thermal conductivity of the composite with 20 wt% TiO_2 decreased by approximately 35%, compared with that without TiO_2.

Conclusions

This paper provides insights into the high temperature microstructure changes of Si_3N_4/silica aerogel composites. At higher heat treatment temperatures, the silica aerogel inside the composite material gradually crystallised, and the fusion of micropores led to pore decrease and pore size increase. Below 700 °C, the thermal diffusivity of the composites remained basically unchanged with the increase of temperature, whereas at $T \geq 1000$ °C the thermal diffusivity and thermal conductivity increased sharply. Si_3N_4/silica aerogel composites were further doped with TiO_2 particles as opacifier, to reduce the radiative thermal conductivity. At higher TiO_2 contents, the thermal diffusivity and thermal conductivity of the composites decreased gradually, with a limited decrease trend below 800 °C and pronounced above 1000 °C. A further increase of TiO_2 content leads to the continuous dielectric constant increase, with consequent dielectric properties of the composite unsuitable to the performance requirements for wave-transmitting applications.

Author contributions

Haixia Yang: writing – original draft, investigation, resources, funding acquisition. Feng Ye: writing – reviewing, investigation, supervision.

Conflicts of interest

There are no conflicts to declare.

Acknowledgements

References

1 D. Yao, H. Chen, K. H. Zuo, Y. Xia, J. Yin, H. Liang and Y. P. Zeng, *Ceram. Int.*, 2018, **44**, 11966–11971.

2 Z. L. Cheng, Y. E. Fang, Y. S. Liu, *et al.*, *J. Adv. Ceram.*, 2019, **8**, 399–407.

3 H. L. Yang, Y. Li, Q. G. Li, Z. Wang, H. Wu, X. F. Liu, Y. Y. Wu and X. Cheng, *Ceram. Int.*, 2020, **46**, 17122–17129.

4 Z. P. Hou, F. Ye and Li. M. Liu, *J. Eur. Ceram. Soc.*, 2015, **35**, 4115–4120.

5 X. Y. Zhang, N. Li, T. Lan, Y. J. Lu, K. Gan, J. M. Wu, W. L. Huo, J. Xu and J. L. Yang, *Ceram. Int.*, 2017, **43**, 4235–4240.

6 S. Komarneni and C. Rutiser, *J. Eur. Ceram. Soc.*, 1996, **16**, 143–147.

7 E. Vinogradova, M. Estrada and A. Moreno, *J. Colloid Interface Sci.*, 2006, **298**, 209–212.

8 H. Maleki, L. Durães and A. Portugal, *J. Non-Cryst. Solids*, 2014, **385**, 55–74.

9 M. F. Bertino, J. F. Hund, J. Sosa, G. Zhang, C. Sotiriou-Leventis, N. Leventis, A. T. Tokuhiro and J. Terry, *J. Non-Cryst. Solids*, 2004, **333**, 108–110.

10 J. Cai, S. L. Liu, J. Feng, S. Kimura, M. Wada, S. Kuga and L. N. Zhang, *Angew. Chem., Int. Ed.*, 2012, **51**, 2076–2079.

11 M. A. B. Meador, B. N. Nguyen, D. Quade and S. L. Vivod, *ACS Appl. Mater. Interfaces*, 2010, **2**, 2162–2168.

12 M. Hajar, D. Luisa and P. Antonio, *Mater. Lett.*, 2016, **179**, 206–209.

13 M. S. Gilani, M. N. Boone, J. L. Fife, S. Y. Zhao, M. M. Koebel, T. Zimmermann and P. Tingaut, *Compos. Sci. Technol.*, 2016, **124**, 71–80.

14 X. B. Tang, A. H. Sun, C. Y. Chu, M. L. Yu, S. Ma, Y. C. Cheng, J. J. Guo and G. J. Xu, *Mater. Des.*, 2017, **115**, 415–421.

15 Z. Niazi, M. Ashjari and Y. Janqamsari, *Microporous Mesoporous Mater.*, 2022, **332**, 111682.

16 Z. H. Yi, X. Zhang, L. W. Yan, X. D. Huyan, T. Zhang, S. Liu, A. R. Guo, J. C. Liu and F. Hou, *Composites, Part B*, 2022, **230**, 109549.

17 X. Zhang, T. Zhang, Z. H. Yi, L. W. Yan, S. Liu, X. H. Yao, A. R. Guo, J. C. Liu and F. Hou, *Ceram. Int.*, 2020, **46**, 28561–28568.

18 M. Afrashi, D. Semnani, Z. Talebi, P. Dehghn and M. Maherolnaghsh, *J. Non-Cryst. Solids*, 2019, **503–504**, 186–193.

19 Z. X. Lu, Z. S. Yuan, Q. Liu, Z. J. Hu, F. Xie and M. Zhu, *Mater. Sci. Eng., A*, 2015, **625**, 278–287.

20 Y. X. Chen, S. Sepahvand, F. Gauvin, K. Schollbach, H. J. H. Brouwers and Q. L. Yu, *Constr. Build. Mater.*, 2021, **293**, 123289.

21 S. P. Patil, *Scr. Mater.*, 2021, **196**, 113757.

22 G. Buscarino, V. Ardizzone, G. Vaccaro and F. M. Gelardi, *J. Non-Cryst. Solids*, 2010, **357**, 1866–1870.

23 H. Yu, Y. Jiang, Y. Lu, X. Li, H. Zhao, Y. Ji and M. Wang, *J. Non-Cryst. Solids*, 2019, **505**, 79–86.

24 G. Zu, J. Shen, L. Zou, W. Zou, Y. Wu and Y. Zhang, *Microporous Mesoporous Mater.*, 2017, **238**, 90–96.

25 Y. G. Kwon, S. Y. Choi, E. S. Kang and S. S. Baek, *J. Mater. Sci.*, 2000, **35**, 6075–6079.

26 P. Jean, D. Florence, C. Sylvie, F. Annelise, D. Philippe, S. Robert and W. Thierry, *Opt. Mater.*, 2004, **26**, 167–172.

27 H. X. Yang, F. Ye, Q. Liu and Y. Gao, *Mater. Des.*, 2015, **85**, 438–443.

28 Y. N. Duan, C. J. Sadhan, L. Bimala and P. E. Matthew, *Langmuir*, 2013, **29**, 6156–6165.